nanomaterials

MDPI

Article

Plasma Enabled Fe_2O_3/Fe_3O_4 Nano-aggregates Anchored on Nitrogen-doped Graphene as Anode for Sodium-Ion Batteries

Qianqian Wang [1], Yujie Ma [1], Li Liu [1], Shuyue Yao [1], Wenjie Wu [1], Zhongyue Wang [1], Peng Lv [1], Jiajin Zheng [1], Kehan Yu [1,*], Wei Wei [1] and Kostya (Ken) Ostrikov [2,3]

1 School of Electronic and Optical Engineering Nanjing University of Posts and Telecommunications, Nanjing 210023, China; wqq1242103532@163.com (Q.W.); 1017030916@njupt.edu.cn (Y.M.); a884205500701@icloud.com (L.L.); ysynn0916@163.com (S.Y.); wuvenjie@163.com (W.W.); zywang@njupt.edu.cn (Z.W.); lvp@njupt.edu.cn (P.L.); zhengjj@njupt.edu.cn (J.Z.); weiwei@njupt.edu.cn (W.W.)

2 School of Chemistry and Physics, Queensland University of Technology, Brisbane QLD 4000, Australia; kostya.ostrikov@qut.edu.au

3 CSIRO-QUT Joint Sustainable Processes and Devices Laboratory P.O. Box 218, Lindfield NSW 2070, Australia

* Correspondence: kehanyu@njupt.edu.cn

Received: 4 April 2020; Accepted: 16 April 2020; Published: 18 April 2020

Abstract: Low electrical conductivity severely limits the application of Fe_2O_3 in lithium- and sodium-ion batteries. In respect of this, we design and fabricate Fe_2O_3/Fe_3O_4 nano-aggregates anchored on nitrogen-doped graphene as an anode for sodium-ion batteries with the assistance of microwave plasma. The highly conductive Fe_3O_4 in the composite can function as a highway of electron transport, and the voids and phase boundaries in the Fe_2O_3/Fe_3O_4 heterostructure facilitate Na^+ ion diffusion into the nano-aggregates. Furthermore, the Fe–O–C bonds between the nano-aggregates and graphene not only stabilize the structural integrity, but also enhance the charge transfer. Consequently, the Fe_2O_3/Fe_3O_4/NG anode exhibits specific capacity up to 362 mAh g^{-1} at 100 mA g^{-1}, excellent rate capability, and stable long-term cycling performance. This multi-component-based heterostructure design can be used in anode materials for lithium- and sodium-ion batteries, and potential opens a new path for energy storage electrodes.

Keywords: iron oxide; graphene; phase boundary; plasma; sodium-ion battery

1. Introduction

Insufficient lithium resources will seriously threaten the availability of future lithium-ion batteries (LIB). Owing to a similar working mechanism to LIBs, abundance, lower price, and environmental friendliness, sodium-ion batteries (SIBs) have gradually become a hotspot for energy storage [1–4]. Advances in SIB technology rely on the selection of suitable electrode materials to accommodate, insert, and extract Na^+ ions with a larger radius than Li^+ [5,6].

Among many metal oxides, the theoretical capacity of Fe_2O_3 is as high as ~1007 mAh g^{-1}, and its environmental friendliness, low cost, and abundant resources make it an ideal anode material for SIBs [7]. However, Fe_2O_3 undergoes a large volume expansion (200%) during charge-discharge, resulting in electrode pulverization and deteriorated electrical contact problems [8,9]. On the other hand, the low electrical conductivity of Fe_2O_3 (10^{-14} S cm^{-1}) and low ionic diffusivity limits the rate performance of batteries [10,11]. Common strategies are to design nanosized iron oxide, and to use conductive additives, such as graphene [9,12,13]. Another iron-based oxide, Fe_3O_4, has a slightly lower specific capacity (926 mAh g^{-1}) and much higher electrical conductivity (10^2~10^3 S cm^{-1}) than Fe_2O_3 [14]. Rationally

compounding Fe_2O_3 and Fe_3O_4 may improve the conductivity, facilitate the redox charge transfer, and thus the rate performance. As has been demonstrated in supercapacitors, the conductive Fe_3O_4 and capacitive Fe_2O_3 synergistically produced excellent rate capability and cycling stability [15–17]. Recently, α-Fe_2O_3/Fe_3O_4 composite, Fe_2O_3/Fe_3O_4/$FeCO_3$ composite, and porous Fe_2O_3/Fe_3O_4@carbon have also been applied in LIBs and exhibited improved electrochemical performance in comparison with the Fe_2O_3 electrodes [18–20]. In these studies, the Fe_3O_4 plays the role of electron transport pathway, while the porous structure can facilitate fast ion transport. It is even claimed that the hetero-interfaces between the oxide components may provide an enhanced inner electric field which can assist the electron transfer and Li^+ diffusion [19].

In this work, we designed Fe_2O_3/Fe_3O_4 nano-aggregates anchored on nitrogen-doped graphene (Fe_2O_3/Fe_3O_4/NG) as an anode of SIBs. Upon a microwave plasma process, the Fe_2O_3/Fe_3O_4/NG composite exhibited rich phase boundaries and voids. When working as an SIB anode material, the Fe_2O_3/Fe_3O_4/NG shows high specific capacity (362 mAh g^{-1} at 100 mA g^{-1}), excellent cycling stability (84% capacity retention after 100 cycles at 1 A g^{-1}), and superior high-rate capability. The improved electrochemical performances are due to fast electron transport through Fe_3O_4, accelerated Na^+ ion transport through Fe_2O_3/Fe_3O_4 phase boundaries, and voids in the nano-aggregates.

2. Materials and Methods

2.1. Materials Preparation

The graphene oxide (GO) used in this work was produced from natural graphite flakes (Acros, Geel, Belgium) by a modified Hummer's method [21]. The aqueous GO dispersion was centrifuged at 11,000 rpm for 30 min and was redispersed in de-ionized (DI) water more than 3 times. By discarding the supernatant, GO suspension in N, N-dimethyl formamide (DMF, 98%, Sigma-Aldrich, St. Louis, MO, USA) with 2 mg mL^{-1} was made.

Fe_2O_3/NG was synthesized by a solvothermal method. $Fe(NO_3)_3{\cdot}9H_2O$ (840 mg, 99.9%, Sigma-Aldrich) was dissolved in the as-obtained GO suspension (100 mL). After stirring for 60 min, the mix was transferred into a Teflon-lined autoclave and was kept at 180 °C for 6 h. The as-obtained gel was rinsed in DI water for 24 h, then freeze-dried at −60 °C, 20 Pa for 24 h to generate Fe_2O_3/NG. The as-prepared bulk Fe_2O_3/NG was ground to powder with a mortar and pestle. After treating in a home-made microwave plasma fluidized bed (power of microwave = 400 W, Ar 40 sccm, H_2 10 sccm, 20 min), Fe_2O_3/Fe_3O_4/NG was obtained.

2.2. Materials Characterization

The crystal structure and phases of the material were characterized by X-ray diffraction (XRD, Bruker AXS GmbH, Karlsruhe, Germany) using Cu-Kα radiation. Morphology was analyzed by a field emission scanning electron microscope (SEM, Hitachi S4800, Tokyo, Japan). The transmission electron microscope (TEM) and high-resolution transmission electron microscope (HRTEM) were performed on a Hitachi HT7700 (Tokyo, Japan) and Talos F200X (Waltham, MA, USA), respectively. Thermogravimetric analysis was performed on PE STA8000 (Waltham, MA, USA). X-ray photoelectron spectroscopy (XPS) was performed on KRATOS Axis Supra XPS system (Kratos, Manchester, UK). The measured binding energies were calibrated to the reference energy by C1s = 284.6 eV. Raman spectroscopy was measured using the RM2000 system (Renishaw, London, UK), using a laser source with 17 mW at 532 nm.

2.3. Electrochemical Measurements

The active material, carbon black, and polyvinylidene fluoride (PVDF, Sigma-Aldrich) were added to N-methyl-2-pyrrolidone (NMP, 98%, Sigma-Aldrich) at a mass ratio of 8: 1: 1, and fully stirred to obtain a slurry. The resulting slurry was applied to copper foil, and dried in a vacuum oven at 100 °C for 12 h to obtain negative electrodes. The total mass loadings on a copper foil (20 mm in diameter, 99.99%,

Sigma-Aldrich) are 1.13 and 0.75 mg for the Fe_2O_3/Fe_3O_4/NG and Fe_2O_3/NG electrodes, respectively. They were electrochemically characterized in CR2016-type coin cells, using Na metal as the counter electrode and reference electrode, and glass microfiber (Whatman, Little Chalfont, UK) as the separator. Dissolving 1 M $NaClO_4$ (98%, Acros) in a mixed solvent of ethylene carbonate (EC, Acros) and diethyl carbonate (DEC, Acros) with 1:1 volume ratio, and adding 5 vol.% of fluoroethylene carbonate (FEC, Acros) additive, the electrolyte was prepared. Galvanostatic charge-discharge were performed on a LAND battery tester (Wuhan, China) in range of 0.01 to 3.0 V (vs. Na/Na^+). Cyclic voltammetry (CV) and electrochemical impedance spectroscopy (EIS) measurements were performed using the CHI660E electrochemical workstation (Shanghai, China). All as-assembled half cells stood in a glove box for 12 h EIS tests without cycling. All capacities were calculated based on the mass of the active materials.

3. Results

The Fe_2O_3/Fe_3O_4/NG nanocomposite was obtained by a solvothermal synthesis of Fe_2O_3/NG followed by a microwave plasma treatment. Taking advantage of the activation ability of plasma, the Fe_2O_3 was partially reduced to the Fe_3O_4, and Fe_2O_3/Fe_3O_4 nanoaggregates were formed, as illustrated in Scheme 1 [22].

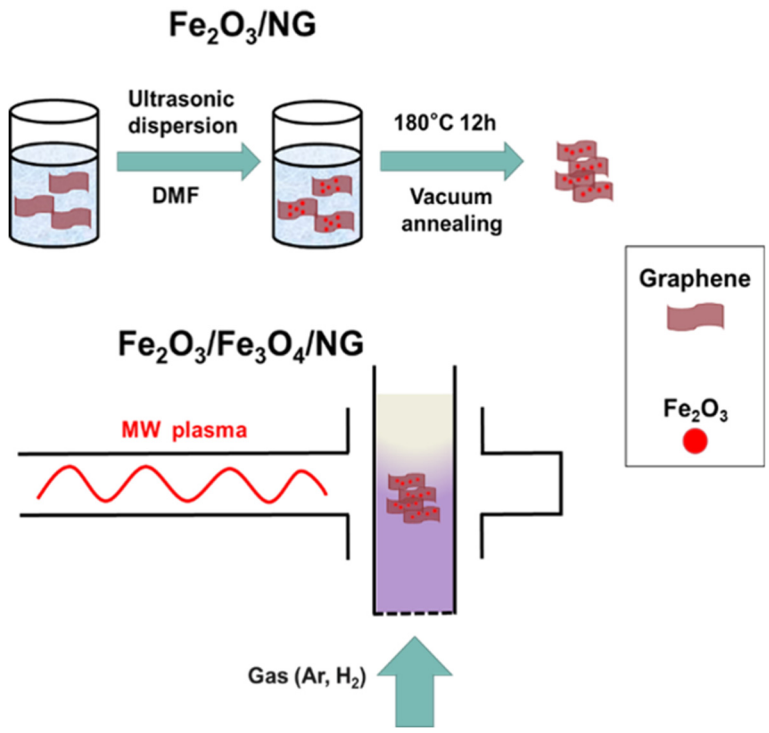

Scheme 1. Schematics of synthesis of Fe_2O_3/NG and Fe_2O_3/Fe_3O_4/NG composites.

As shown in the SEM and TEM images (Figure 1a,b), Fe_2O_3 nanoparticles with size around 50 nm are well enveloped in graphene in the Fe_2O_3/NG composite. After plasma radiation, the morphology of the composite and the particle size distribution showed no significant change (Figure 1c and the inset). Under TEM observation, however, the previous spherical or ellipsoidal particles turned out to be in irregular shape. Meanwhile, dark and bright areas can be differentiated, of which the bright area is perhaps voids in the particles (Figure 1d). HRTEM reveals that the inhomogeneity of the particles stems from phase segregation of Fe_2O_3 and Fe_3O_4. In a close view of a particle, fringe spacing of 0.37 nm (corresponding to (012) plane of Fe_2O_3) and 0.29 nm (corresponding to the (220) plane of Fe_3O_4) can be found simultaneously (Figure 1e). The results confirmed that the Fe_2O_3 was partially reduced to Fe_3O_4 by energetic species in the plasma. Driven by phase segregation, Fe_2O_3/Fe_3O_4 nano-aggregates were eventually formed. The mass fraction of active materials ise about 87 and

80 wt.% for Fe_2O_3/Fe_3O_4/NG and Fe_2O_3/NG, respectively, as calculated from the thermal-gravimetric analysis and differential thermal analysis (TGA/DTA) results (Figure 1f).

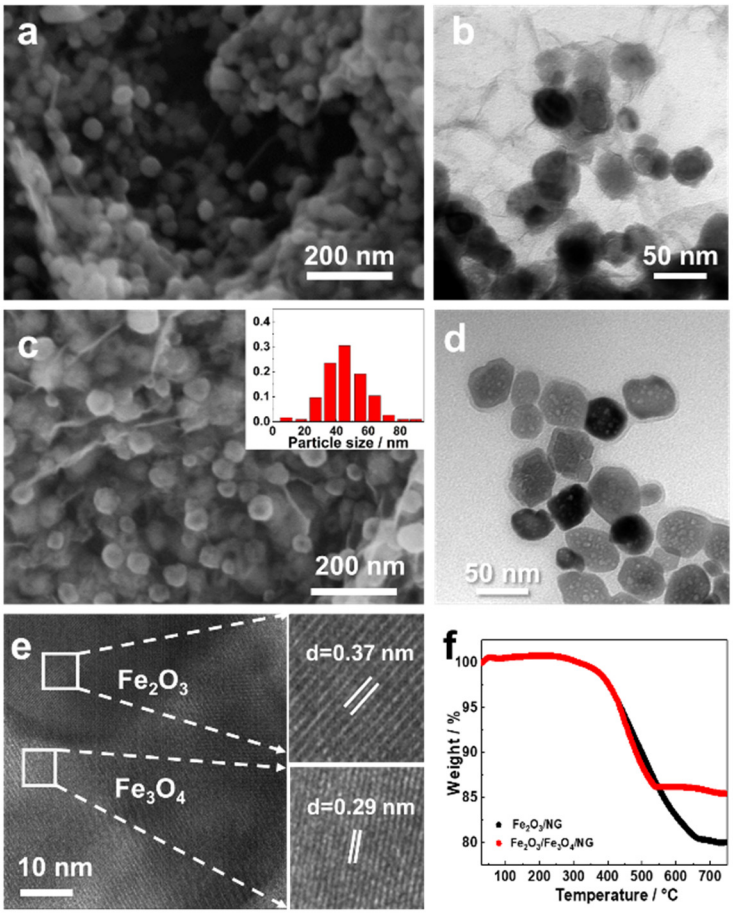

Figure 1. (**a**,**b**) SEM, TEM images of Fe_2O_3/NG composites. (**c**,**d**) SEM, TEM images of Fe_2O_3/Fe_3O_4/NG composites. The inset shows particle size distribution of Fe_2O_3/Fe_3O_4. (**e**) An HRTEM image of a Fe_2O_3/Fe_3O_4 particle, the right two panels denote interplane spacings of Fe_2O_3 and Fe_3O_4. (**f**) TGA curves of Fe_2O_3/NG and Fe_2O_3/Fe_3O_4/NG composites.

XRD analysis shows diffraction peaks at 24.13, 33.15, 35.61, 40.85, 49.48, 54.09, 62.45, and 63.9° for the Fe_2O_3/NG (Figure 2a), which are corresponding to the (012), (104), (110), (113), (024), (116), (214), and (300) planes of Fe_2O_3 (PDF No.33-0664), respectively. For the Fe_2O_3/Fe_3O_4/NG, additional peaks at 30.07, 37.05, and 47.13° can be found, which are corresponding to the (220), (222), and (331) planes of Fe_3O_4 (PDF No 99-0073), respectively, confirming coexistence of Fe_2O_3 and Fe_3O_4 phases (Figure 2a). The Raman D peak of RGO are upshifted from 1340 (RGO) to 1343 cm^{-1} (NG) and G peak from 1573 to 1576 cm^{-1} after N doping (Figure 2b). This may be due to the strain of the graphene basal plane caused by C–N bond, indicating the successful insertion of nitrogen heteroatoms [23]. Additionally, the unchanged Raman spectrum after microwave plasma process indicates stable N doping upon plasma (red curve in Figure 2b).

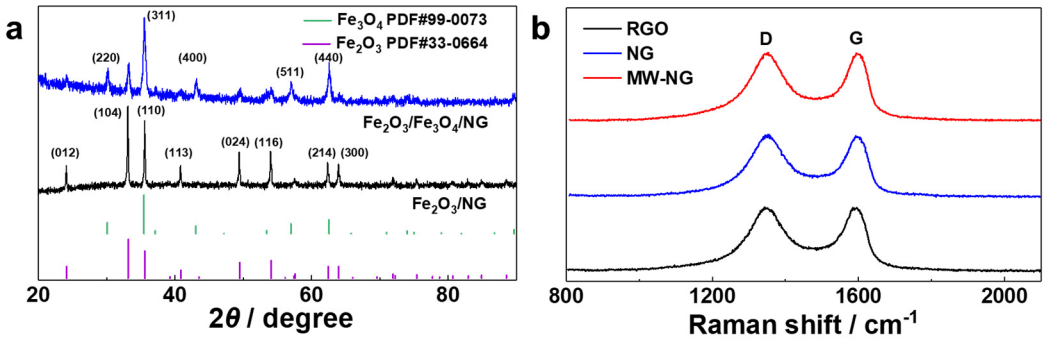

Figure 2. (**a**) XRD patterns of Fe_2O_3/Fe_3O_4/NG and Fe_2O_3/NG composites. (**b**) Raman spectra of microwave processed NG (MW-NG), NG, and RGO in the range of 1000–1800 cm^{-1}.

XPS survey scans discovered Fe 2p, O 1s, N 1s, and C 1s states in both Fe_2O_3/Fe_3O_4/NG and Fe_2O_3/NG (Figure 3a). In Figure 3b, the high-resolution Fe 2p spectra of the composites have two main peaks at 711.2 and 724.7 eV, corresponding to Fe $2p_{3/2}$ and Fe $2p_{1/2}$, respectively. In the Fe_2O_3/NG, the Fe 2p spectrum consists of a series of characteristic peaks of Fe^{3+} in Fe_2O_3, which are two spin energy separated components (Fe^{3+} (oh) at 711.1 and 725.1 eV), Fe $2p_{3/2}$ satellite (719.7 eV), and Fe $2p_{1/2}$ satellite (733.8 eV) signals, but no F^0e or Fe^{2+} signal is observed. The Fe_2O_3/Fe_3O_4/NG has not only the same components with Fe_2O_3/NG, but also Fe^{2+} (oh), Fe^{3+}(td), Fe^{2+}(oh), and Fe^{3+}(td) signals of Fe_3O_4 at 710.0, 713.0, 723.6, and 727.3 eV, respectively [17]. The XPS analysis clearly evidences the coexistence of Fe_2O_3 and Fe_3O_4 in the hybrid material. With the component area ratio of Fe^{2+} to Fe^{3+}, the atomic ratio of Fe^{2+} to Fe^{3+} can be estimated to be 0.102. Combined with the TGA results, the mass loading of Fe_2O_3 and Fe_3O_4 are calculated to be 0.61 and 0.23 mg, respectively, as described in the Supporting Information for detail.

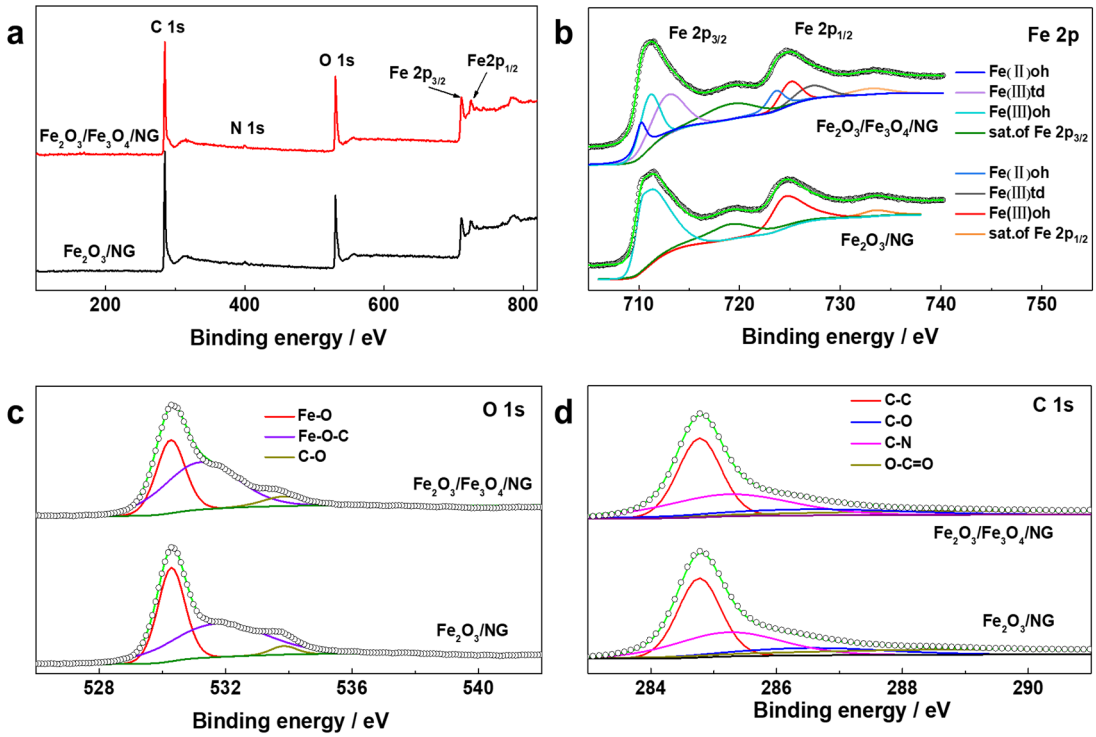

Figure 3. (**a**) XPS spectra of Fe_2O_3/Fe_3O_4/NG and Fe_2O_3/NG. The corresponding (**b**) Fe 2p spectra, (**c**) O 1s spectra, and (**d**) C 1s spectra.

As shown in Figure 3c, the deconvolution of the O 1s profiles reveals three components, Fe–O (530.2 eV), Fe–O–C (531.2 eV), and C–O (533.8 eV). The areal percentage of the Fe–O–C bonds component increases from 53.5% for the Fe_2O_3/NG to 58% for the Fe_2O_3/Fe_3O_4/NG. The additional Fe–O–C bonds can not only promote the electron transport in the Fe_2O_3/Fe_3O_4/NG, but also stabilize the Fe_2O_3/Fe_3O_4 on the graphene sheet during charge/discharge, thereby improving the electrochemical kinetics and stability. [24] In Figure 3d, deconvolution of the C 1s profiles of the nanostructured hybrid material reveals four components including C–C (284.7 eV), C–N (285.2 eV), C–O(286.5 eV), and O–C=O (289.35 eV) [25,26], which remain unchanged before and after the plasma process, except for a slight areal ratio decrease of the O–C=O bonds from 22.78% for the Fe_2O_3/NG to 16.64% for the Fe_2O_3/Fe_3O_4/NG.

The CV curves from the 2nd to the 4th cycle of the electrodes are shown in Figure 4a,b. In the cathodic sweeps, a peak around 1.2 V for the Fe_2O_3/Fe_3O_4/NG in Figure 4a can be assigned to the reduction of Fe^{2+}/Fe^{3+} to Fe^0 (Equations (1) and (2)), while the peak around 0.9 V for the Fe_2O_3/NG in Figure 4b corresponds to the reduction of Fe^{3+} to Fe^0 (Equation (1)). In the anodic sweeps, broad anodic peaks around 1.5 V are ascribed to the oxidation of Fe^0 to Fe^{3+} for both electrodes (insets in Figure 4a,b) [24,27]. Only the Fe_2O_3/Fe_3O_4/NG electrode has a small shoulder peak at 0.8 V (inset in Figure 4a), which is an indication of the oxidization of Fe^0 to Fe^{2+} [19]. The lower peak-to-peak separation between the redox peaks and better coincidence of the sweeps of the Fe_2O_3/Fe_3O_4/NG suggest faster charge transfer kinetics and better reversibility.

$$Fe_2O_3 + 6\,Na^+ + 6\,e^- \longleftrightarrow 2\,Fe^0 + 3\,Na_2O \quad (1)$$

$$Fe_3O_4 + 8\,Na^+ + 8\,e^- \longleftrightarrow 3\,Fe^0 + 4\,Na_2O \quad (2)$$

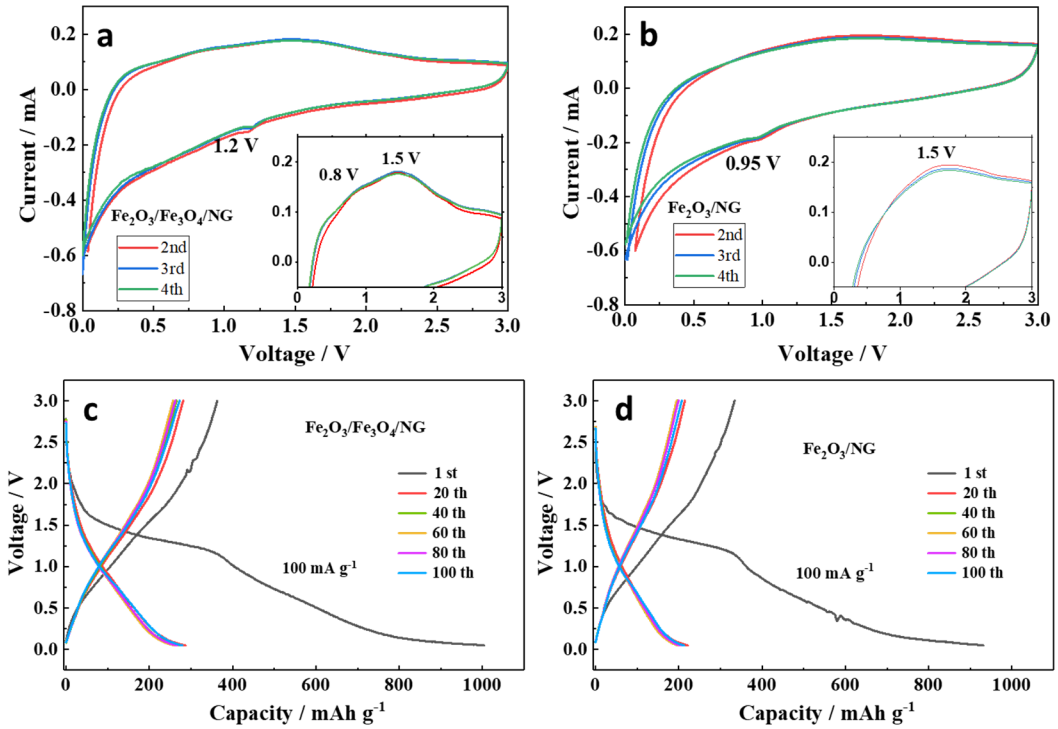

Figure 4. CV curves of (**a**) Fe_2O_3/Fe_3O_4/NG and (**b**) Fe_2O_3/NG anodes from the 2nd to 4th cycle at a scan rate of 1.0 mV s^{-1} between 0.05 and 3 V vs. Na/Na^+. Galvanostatic charge-discharge curves of (**c**) Fe_2O_3/Fe_3O_4/NG and (**d**) Fe_2O_3/NG anodes at a current density of 100 mA g^{-1}.

Figure 4c,d shows charge–discharge curves of the two types of electrodes at a current density of 100 mA g^{-1} in the voltage window of 0.05–3.0 V (vs. Na/Na^+). The initial specific discharge and charge capacities of the Fe_2O_3/NG electrode are 931 and 334 mAh g^{-1}, respectively, with an initial

coulombic efficiency of 36%. After the microwave plasma process, the obtained Fe_2O_3/Fe_3O_4/NG composite exhibits initial specific discharge capacity of 1004 mAh g^{-1}, charge capacity of 363 mAh g^{-1}, and an almost identical initial coulombic efficiency. The lost capacity mainly stems from the formation of SEI and probably degradation of the electrolyte. In the subsequent discharge–charge cycles, the Fe_2O_3/Fe_3O_4/NG electrode has significantly higher capacities than the Fe_2O_3/NG.

The rate performances of Fe_2O_3/NG and Fe_2O_3/Fe_3O_4/NG electrodes are compared in Figure 5a. With progressively growing current density from 100 to 1200 mA g^{-1}, the Fe_2O_3/Fe_3O_4/NG composite constantly exhibits higher discharge capacities than the Fe_2O_3/NG. After a series of cycles, a reversible discharge capacity of 305 mAh g^{-1} at 100 mA g^{-1} is reached for the Fe_2O_3/Fe_3O_4/NG, comparing with 239 mAh g^{-1} for the Fe_2O_3/NG. The specific capacity contributed by Fe_2O_3 in the Fe_2O_3/Fe_3O_4/NG can be estimated by the XPS and TGA results. For example, the reversible capacity contributed by Fe_2O_3 after the rate performance testing at 100 mA g^{-1} can be 307–358 mAh g^{-1}, which is higher than the 239 mAh g^{-1} for the Fe_2O_3/NG. This evidently suggests a synergetic effect of Fe_2O_3 and Fe_3O_4 in the electrode. The calculation of capacity contributed by Fe_2O_3 is detailed in the Supporting Information.

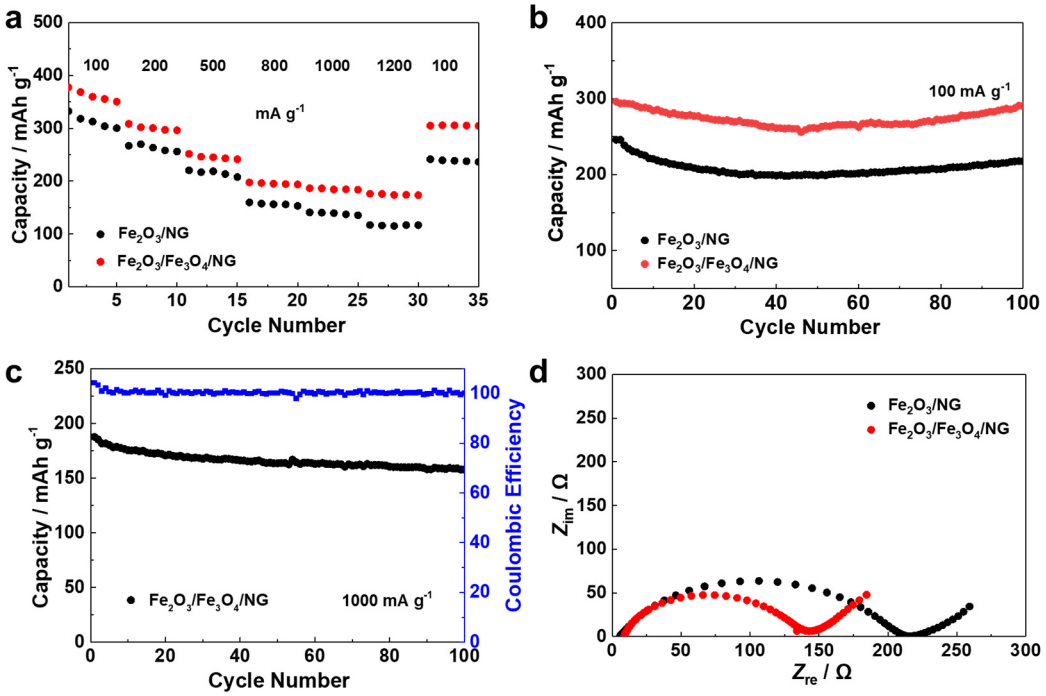

Figure 5. (**a**) Rate performance of Fe_2O_3/NG and Fe_2O_3/Fe_3O_4/NG tested at current densities from 100 to 1200 mA g^{-1}. (**b**) Cycling performances of Fe_2O_3/NG and Fe_2O_3/Fe_3O_4/NG at current density of 100 mA g^{-1}. (**c**) Cycling performance of Fe_2O_3/Fe_3O_4/NG at current density of 1000 mA g^{-1}. (**d**) Nyquist plots of electrochemical impedance spectra (EIS) of Fe_2O_3/NG and Fe_2O_3/Fe_3O_4/NG.

In Figure 5b, the cycling performance of Fe_2O_3/NG and Fe_2O_3/Fe_3O_4/NG electrodes in 100 cycles are compared at a current density of 100 mA g^{-1}. After 100 cycles, the capacity of Fe_2O_3/Fe_3O_4/NG is 291 mAh g^{-1}, which is much higher than that of Fe_2O_3/NG 218 mAh g^{-1}. At a higher current density (1000 mA g^{-1}), Fe_2O_3/Fe_3O_4/NG can still discharge 158 mAh g^{-1} after 100 cycles (capacity retention rate 84%, Figure 5c).

In Figure 5d, the electrochemical impedance spectra (EIS) Nyquist plots of Fe_2O_3/NG and Fe_2O_3/Fe_3O_4/NG electrodes present a depressed semicircle in the high-frequency region and a straight line in the low-frequency region. To extract the EIS parameters, an equivalent circuit is proposed, as displayed in Supplementary Figure S1. The EIS tests were performed before cycling of the electrodes, with open circuity voltages of 1.65 and 1.47 V for the Fe_2O_3/NG and Fe_2O_3/Fe_3O_4/NG, respectively. As listed in Table 1, both cells present similar values of electrolyte resistance (R_s). The Fe_2O_3/Fe_3O_4/NG

electrode has a charge transfer resistance (R_{ct}: 134.6 Ω) that is only half of the Fe_2O_3/NG (210.7 Ω). The reduction of the semicircle (or R_{ct}) is due to more Fe-O-C bonds and the appearance of Fe_3O_4 in the electrode, indicating that the charge transfer kinetics in Fe_2O_3/Fe_3O_4/NG is faster. Moreover, the one order of magnitude higher diffusion coefficient of Na^+ (D_{Na^+}, obtained by fitting the EIS, see Supporting Information for detail) in the Fe_2O_3/Fe_3O_4/NG can be attributed to the fast Na^+ diffusion through the phase boundaries and voids in the Fe_2O_3/Fe_3O_4 heterostructure.

Table 1. The fitted EIS parameters and diffusion coefficients of Fe_2O_3/NG and Fe_2O_3/Fe_3O_4/NG.

Electrode	R_s (Ω)	R_{ct} (Ω)	D_{Na^+} ($cm^2\ s^{-1}$)
Fe_2O_3/NG	6	210.6	1.65×10^{-12}
Fe_2O_3/Fe_3O_4/NG	8.9	134.7	1.34×10^{-11}

The long-term cycling performance is elucidated by post-mortem observation, as shown in Figure 6. Serious cracks and particle swelling can be observed for the Fe_2O_3/NG electrode after 100 discharge-charge cycles at 1000 mA g^{-1} (Figure 6a,b). By contrast, in the same condition, the Fe_2O_3/Fe_3O_4/NG electrode remained almost unchanged in terms of particle shape and size (Figure 6c,d). In a word, the comparison clearly demonstrates the stabilizing effect of the Fe_2O_3/Fe_3O_4/NG electrodes structure. Even after 300 cycles, the Fe_2O_3/Fe_3O_4/NG electrode could retain its particle size, although cracks occurred (Figure 6e,f).

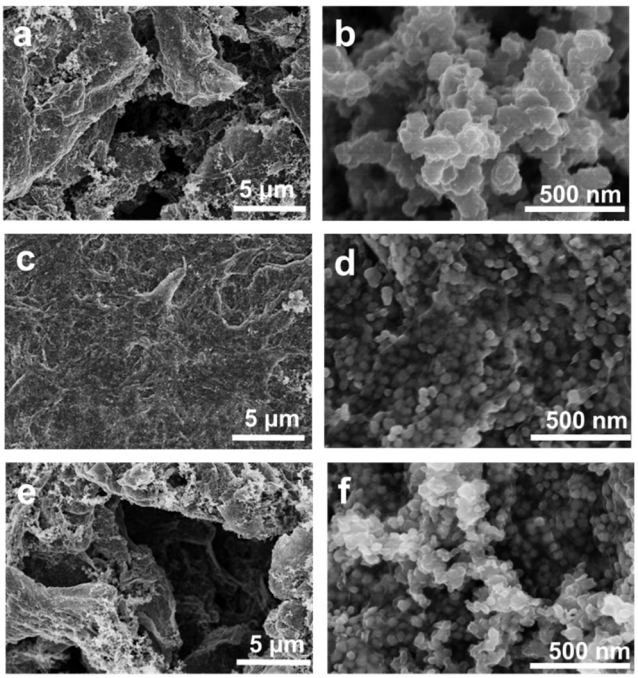

Figure 6. SEM images of the (**a**,**b**) Fe_2O_3/NG and (**c**,**d**) Fe_2O_3/Fe_3O_4/NG electrodes after 100 discharge-charge cycles at 1000 mA g^{-1} at different magnifications. SEM images of the (**e**,**f**) Fe_2O_3/Fe_3O_4/NG electrodes after 300 discharge–charge cycles at 1000 mA g^{-1} at different magnifications.

4. Discussion

The outstanding sodium storage properties of the Fe_2O_3/Fe_3O_4/NG can be attributed to its unique structural features, as illustrated in Scheme 2. First, the highly conductive Fe_3O_4 improves electron transport in the hybrid Fe_2O_3/Fe_3O_4 nano-aggregates. Second, the phase boundaries and voids in the Fe_2O_3/Fe_3O_4 heterostructure provide fast diffusion channels for Na^+ ions. Third, the robust interfacial interaction reinforced by Fe–O–C bonds can not only maintain the integrity of the electrode during the long-term cycles, but also provide a highway for electron transfer between the graphene and the

Fe_2O_3/Fe_3O_4 nano-aggregates. Moreover, N-doping also assists the sodium storage, increasing the reversible capacity of materials. All these structural features endowed by the microwave plasma process lead to outstanding reversible capacity, good rate performance, and long-term cycling stability. As compared in Table 2, the electrochemical performance of the Fe_2O_3/Fe_3O_4/NG is among the top-ranking of the reported iron oxide/graphene-based SIB anodes.

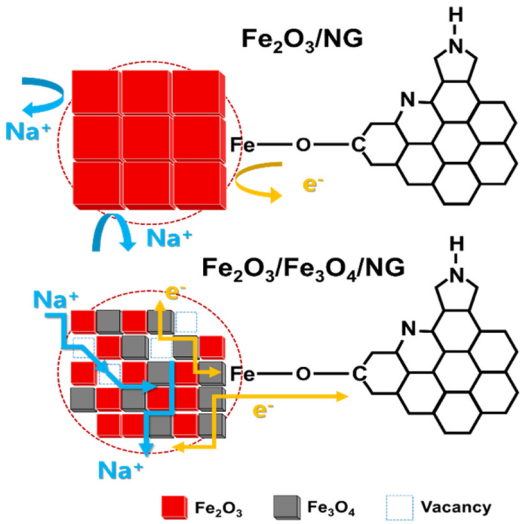

Scheme 2. Schematics of structures, electron transfer and transport, and ion diffusion in Fe_2O_3/NG (upper) and Fe_2O_3/Fe_3O_4/NG (lower) composites.

Table 2. Comparison of the specific capacities of iron oxide based anodes in literature and Fe_2O_3/Fe_3O_4/NG anode in this work.

Anodes	Current Density (mA g^{-1})				References
	Capacity (mAh g^{-1})				
Fe_2O_3/Fe_3O_4/NG	100 362	200 300	1000 185	1200 174	This work
Fe_2O_3/NG	50 343	100 285	200 230	1000 132	Meng 2017 [28]
Fe_2O_3/C	50 364	100 291	200 245	1000 150	Zhang 2018 [29]
Fe_3O_4/G	100 310	200 225	500 180	1000 140	Fu 2016 [30]
Fe_3O_4@C/G	100 375	200 300	500 254	1000 200	Qi 2019 [31]
Fe_2O_3@NC	200 289	500 253.7	1000 221.5	4000 167.8	Guo 2018 [32]
Fe_3O_4/G/QD	100 316	200 273	500 216	1000 113	Liu 2016 [33]
Fe_3O_4/C	100 293	200 262	500 223	1000 195	Wang 2017 [34]
Fe_3O_4@N–C	80 386	240 315	400 277	800 248	Zhao 2019 [35]

5. Conclusions

In summary, the Fe_2O_3/Fe_3O_4 nano-aggregates anchored on nitrogen-doped graphene as an anode for sodium-ion batteries were successfully prepared with the assistance of the microwave plasma process.

The highly conductive Fe_3O_4 in the composite improves electron transport, and the voids and phase boundaries facilitate Na^+ ion diffusion into the Fe_2O_3/Fe_3O_4 heterostructure. Moreover, the Fe–O–C bonds not only strength the structural robustness, but also electrically bridge the graphene and the Fe_2O_3/Fe_3O_4 nano-aggregates. Consequently, the Fe_2O_3/Fe_3O_4/NG anode exhibits outstanding electrochemical performance, i.e., high specific capacity, excellent rate capability, and stable long-term cycling performance. The design concept of this unique heterostructure can be extended to other energy storage applications based on metal oxides.

Supplementary Materials: The following are available online at http://www.mdpi.com/2079-4991/10/4/782/s1, Figure S1: (a) the equivalent electrical circuit (b,c) The Z'-$\omega^{-1/2}$ plots for the Fe_2O_3/NG and Fe_2O_3/Fe_3O_4/NG. Table S1. Calculation of capacity contributed by Fe_2O_3 in the Fe_2O_3/Fe_3O_4/NG electrode.

Author Contributions: Formal analysis, L.L., S.Y. and W.W. (Wenjie Wu); investigation, Q.W., Y.M., L.L., S.Y., W.W. (Wenjie Wu), Z.W. and P.L.; writing—original draft preparation, Q.W.; writing—review and editing, K.Y., Y.M. and K.O.; supervision, J.Z. and K.Y.; project administration, K.Y.; funding acquisition, W.W. (Wei Wei); resources, W.W. (Wei Wei). All authors have read and agreed to the published version of the manuscript.

Funding: This work was funded by the Program of Distinguished Professor of Jiangsu Province.

Acknowledgments: We thank Zhenhai Wen at Fujian Institute of Research on the Structure of Matter Chinese Academy of Sciences for the assistance with electrochemical analysis. K.O. thanks the Australian Research Council for partial support. L.L. thanks the Postgraduate Research & Practice Innovation Program of Jiangsu Province, China (Grant No. KYCX18_0853) for partial support.

Conflicts of Interest: The authors declare no conflict of interest.

References

1. Xiao, L.F.; Lu, H.Y.; Fang, Y.J.; Sushko, M.L.; Cao, Y.L.; Ai, X.P.; Yang, H.X.; Liu, J. Low-Defect and Low-Porosity Hard Carbon with High Coulombic Efficiency and High Capacity for Practical Sodium Ion Battery Anode. *Adv. Energy Mater.* **2018**, *8*, 7. [CrossRef]
2. Sun, W.P.; Rui, X.H.; Zhang, D.; Jiang, Y.Z.; Sun, Z.Q.; Liu, H.K.; Dou, S.X. Bismuth sulfide: A high-capacity anode for sodium-ion batteries. *J. Power Sources* **2016**, *309*, 135–140. [CrossRef]
3. Pan, H.L.; Hu, Y.S.; Chen, L.Q. Room-temperature stationary sodium-ion batteries for large-scale electric energy storage. *Energy Environ. Sci.* **2013**, *6*, 2338–2360. [CrossRef]
4. Ponrouch, A.; Marchante, E.; Courty, M.; Tarascon, J.M.; Palacin, M.R. In search of an optimized electrolyte for Na-ion batteries. *Energy Environ. Sci.* **2012**, *5*, 8572–8583. [CrossRef]
5. Hwang, J.Y.; Myung, S.T.; Sun, Y.K. Sodium-ion batteries: Present and future. *Chem. Soc. Rev.* **2017**, *46*, 3529–3614. [CrossRef]
6. Yabuuchi, N.; Kubota, K.; Dahbi, M.; Komaba, S. Research Development on Sodium-Ion Batteries. *Chem. Rev.* **2014**, *114*, 11636–11682. [CrossRef]
7. Chen, J.; Xu, L.N.; Li, W.Y.; Gou, X.L. alpha-Fe_2O_3 nanotubes in gas sensor and lithium-ion battery applications. *Adv. Mater.* **2005**, *17*, 582–586. [CrossRef]
8. Zhang, N.; Han, X.P.; Liu, Y.C.; Hu, X.F.; Zhao, Q.; Chen, J. 3D Porous gamma-Fe_2O_3@C Nanocomposite as High-Performance Anode Material of Na-Ion Batteries. *Adv. Energy Mater.* **2015**, *5*, 7. [CrossRef]
9. Jian, Z.L.; Zhao, B.; Liu, P.; Li, F.J.; Zheng, M.B.; Chen, M.W.; Shi, Y.; Zhou, H.S. Fe_2O_3 nanocrystals anchored onto graphene nanosheets as the anode material for low-cost sodium-ion batteries. *Chem. Commun.* **2014**, *50*, 1215–1217. [CrossRef]
10. Cui, Z.M.; Hang, L.Y.; Song, W.G.; Guo, Y.G. High-Yield Gas-Liquid Interfacial Synthesis of Highly Dispersed Fe_3O_4 Nanocrystals and Their Application in Lithium-Ion Batteries. *Chem. Mater.* **2009**, *21*, 1162–1166. [CrossRef]
11. Zhu, Q.; Chen, N.; Tao, F.; Pan, Q.M. Improving the lithium storage properties of Fe_2O_3@C nanoparticles by superoleophilic and superhydrophobic polysiloxane coatings. *J. Mater. Chem.* **2012**, *22*, 15894–15900. [CrossRef]
12. Zhang, Z.J.; Wang, Y.X.; Chou, S.L.; Li, H.J.; Liu, H.K.; Wang, J.Z. Rapid synthesis of alpha-Fe_2O_3/rGO nanocomposites by microwave autoclave as superior anodes for sodium-ion batteries. *J. Power Sources* **2015**, *280*, 107–113. [CrossRef]

13. Liu, X.J.; Chen, T.Q.; Chu, H.P.; Niu, L.Y.; Sun, Z.; Pan, L.K.; Sun, C.Q. Fe_2O_3-reduced graphene oxide composites synthesized via microwave-assisted method for sodium ion batteries. *Electrochim. Acta* **2015**, *166*, 12–16. [CrossRef]
14. Zhao, C.J.; Shao, X.X.; Zhang, Y.X.; Qian, X.Z. Fe_2O_3/Reduced Graphene Oxide/Fe_3O_4 Composite in Situ Grown on Fe Foil for High-Performance Supercapacitors. *ACS Appl. Mater. Interfaces* **2016**, *8*, 30133–30142. [CrossRef] [PubMed]
15. Chen, D.J.; Li, S.X.; Xu, B.Y.; Zheng, F.Y.; Zhou, H.F.; Yu, H.W.; Lin, F.; Zhu, X.Q. Polycrystalline iron oxide nanoparticles prepared by C-dot-mediated aggregation and reduction for supercapacitor application. *RSC Adv.* **2016**, *6*, 45023–45030. [CrossRef]
16. Tang, X.; Jia, R.Y.; Zhai, T.; Xia, H. Hierarchical Fe_3O_4@Fe_2O_3 Core-Shell Nanorod Arrays as High-Performance Anodes for Asymmetric Supercapacitors. *ACS Appl. Mater. Interfaces* **2015**, *7*, 27518–27525. [CrossRef]
17. Mallick, S.; Jana, P.P.; Raj, C.R. Asymmetric Supercapacitor Based on Chemically Coupled Hybrid Material of Fe_2O_3-Fe_3O_4 Heterostructure and Nitrogen-Doped Reduced Graphene Oxide. *Chemelectrochem* **2018**, *5*, 2348–2356. [CrossRef]
18. Wang, X.L.; Qin, M.L.; Fang, F.; Jia, B.R.; Wu, H.Y.; Qu, X.H.; Volinsky, A.A. Solution combustion synthesis of nanostructured iron oxides with controllable morphology, composition and electrochemical performance. *Ceram. Int.* **2018**, *44*, 4237–4247. [CrossRef]
19. Huang, Y.; Li, Y.W.; Huang, R.S.; Yao, J.H. Ternary Fe_2O_3/Fe_3O_4/$FeCO_3$ Composite as a High-Performance Anode Material for Lithium-Ion Batteries. *J. Phys. Chem. C* **2019**, *123*, 12614–12622. [CrossRef]
20. Li, Y.F.; Fu, Y.Y.; Chen, S.H.; Huang, Z.Z.; Wang, L.; Song, Y.H. Porous Fe_2O_3/Fe_3O_4@Carbon octahedron arrayed on three-dimensional graphene foam for lithium-ion battery. *Compos. Part B* **2019**, *171*, 130–137. [CrossRef]
21. Hummers, W.S.; Offeman, R.E. Preparation of Graphitic Oxide. *J. Am. Chem. Soc.* **1958**, *80*, 1339. [CrossRef]
22. Vasilev, K.; Ramiasa, M.M. Nanoengineered Interfaces, Coatings, and Structures by Plasma Techniques. *Nanomaterials* **2017**, *7*, 449. [CrossRef] [PubMed]
23. Tan, C.; Cao, J.; Khattak, A.M.; Cai, F.; Jiang, B.; Yang, G.; Hu, S. High-performance tin oxide-nitrogen doped graphene aerogel hybrids as anode materials for lithium-ion batteries. *J. Power Sources* **2014**, *270*, 28–33. [CrossRef]
24. Li, D.; Zhou, J.S.; Chen, X.H.; Song, H.H. Amorphous Fe_2O_3/Graphene Composite Nanosheets with Enhanced Electrochemical Performance for Sodium-Ion Battery. *ACS Appl. Mater. Interfaces* **2016**, *8*, 30899–30907. [CrossRef] [PubMed]
25. Jiang, W.S.; Yang, C.; Chen, G.X.; Yan, X.Q.; Chen, S.N.; Su, B.W.; Liu, Z.B.; Tian, J.G. Preparation of high-quality graphene using triggered microwave reduction under an air atmosphere. *J. Mater. Chem. C* **2018**, *6*, 1829–1835. [CrossRef]
26. Abe, T.; Miyazawa, A.; Kawanishi, Y.; Konno, H. Microwave-Assisted Synthesis of Metal Complexes. *Mini-Rev. Org. Chem.* **2011**, *8*, 315–333. [CrossRef]
27. Zhou, K.; Zhen, Y.; Hong, Z.; Guo, J.; Huang, Z. Enhanced sodium ion batteries performance by the phase transition from hierarchical Fe_2O_3 to Fe_3O_4 hollow nanostructures. *Mater. Lett.* **2017**, *190*, 52–55. [CrossRef]
28. Meng, S.; Zhao, D.-L.; Wu, L.-L.; Ding, Z.-W.; Cheng, X.-W.; Hu, T. Fe_2O_3/nitrogen-doped graphene nanosheet nanocomposites as anode materials for sodium-ion batteries with enhanced electrochemical performance. *J. Alloy. Compd.* **2018**, *737*, 130–135. [CrossRef]
29. Zhang, Y.; Bakenov, Z.; Tan, T.; Huang, J. Synthesis of Core-Shell Carbon Encapsulated Fe_2O_3 Composite through a Facile Hydrothermal Approach and Their Application as Anode Materials for Sodium-Ion Batteries. *Metals* **2018**, *8*, 461. [CrossRef]
30. Fu, Y.; Wei, Q.; Wang, X.; Zhang, G.; Shu, H.; Yang, X.; Tavares, A.C.; Sun, S. A facile synthesis of Fe_3O_4 nanoparticles/graphene for high-performance lithium/sodium-ion batteries. *RSC Adv.* **2016**, *6*, 16624–16633. [CrossRef]
31. Qi, H.; Cao, L.; Li, J.; Huang, J.; Xu, Z.; Jie, Y.; Wang, C. Thin Carbon Layer Coated Porous Fe_3O_4 Particles Supported by rGO Sheets for Improved Stable Sodium Storage. *Chemistryselect* **2019**, *4*, 2668–2675. [CrossRef]
32. Guo, T.X.; Liao, H.X.; Ge, P.; Zhang, Y.; Tian, Y.Q.; Hong, W.W.; Shi, Z.D.; Shao, C.S.; Hou, H.S.; Ji, X.B. Fe_2O_3 embedded in the nitrogen-doped carbon matrix with strong C-O-Fe oxygen-bridge bonds for enhanced sodium storages. *Mater. Chem. Phys.* **2018**, *216*, 58–63. [CrossRef]
33. Liu, H.; Jia, M.Q.; Zhu, Q.Z.; Cao, B.; Chen, R.J.; Wang, Y.; Wu, F.; Xu, B. 3D-0D Graphene-Fe_3O_4 Quantum Dot Hybrids as High-Performance Anode Materials for Sodium-Ion Batteries. *ACS Appl. Mater. Interfaces* **2016**, *8*, 26878–26885. [CrossRef] [PubMed]

34. Wang, N.; Liu, Q.; Li, Y.; Chen, J.; Gu, J.; Zhang, W.; Zhang, D. Self-crosslink assisted synthesis of 3D porous branch-like Fe_3O_4/C hybrids for high-performance lithium/sodium-ion batteries. *RSC Adv.* **2017**, *7*, 50307–50316. [CrossRef]
35. Zhao, Y.J.; Wang, F.X.; Wang, C.; Wang, S.; Wang, C.Y.; Zhao, Z.W.; Duan, L.L.; Liu, Y.P.; Wu, Y.P.; Li, W.; et al. Encapsulating highly crystallized mesoporous Fe_3O_4 in hollow N-doped carbon nanospheres for high-capacity long-life sodium-ion batteries. *Nano Energy* **2019**, *56*, 426–433. [CrossRef]